Composites Part B 137 (2018) 111–122

Contents lists available at ScienceDirect

Composites Part B

journal homepage: www.elsevier.com/locate/compositesb

An incremental inverse analysis procedure for identification of bond-slip laws in composites applied to textile reinforced concrete

Yingxiong Li*, Jan Bielak, Josef Hegger, Rostislav Chudoba

Institute of Structural Concrete, RWTH Aachen University, Aachen, Germany

ARTICLE INFO

Keywords:
Fabrics/textiles
Fibre/matrix bond
Finite element analysis (FEA)
Mechanical testing

ABSTRACT

Textile reinforced concrete (TRC) is a novel composite building material, its structural behavior is substantially influenced by the bond interface between the reinforcing textile fabrics and concrete. The bond interface can be characterized by a nonlinear bond-slip law. The pull-out test is a common experimental procedure for determination of the bond-slip law. In this paper, a general finite element procedure is proposed to calibrate the bond-slip law according to the results of pull-out tests. By adopting a generic multilinear bond-slip law and solving each piece of the law sequentially, the conventional curve fitting procedures employing optimization algorithms, which are computationally expensive and sometimes non-convergent, can be avoided. Pull-out tests of TRC specimens with varying anchorage lengths were carried out and the test results were used as the input data for the calibration procedure. It is found that the calibrated bond-slip law is independent of the specimen length. Using the calibrated bond-slip laws, the pull-out force vs. displacement curves are numerically reproduced. The numerical results agree well with the experimental data.

1. Introduction

Compared to the conventional steel reinforcement, textile fabrics made of carbon, aramid, glass or basalt fiber bundles have higher strength and better corrosion resistance. These advantageous properties enable the production of thin and lightweight TRC components [1,2]. The bond between the reinforcing textile and concrete is one of the key factors determining the macroscopic behavior of the composite [3–6]. A common way in modelling the composite materials for construction is to represent the bond behavior by a bond-slip law, i.e., the shear stress in the interface as a function of the relative slip between matrix and reinforcement [7–16]. The pull-out test has become a quasi-standard procedure to determine such bond-slip laws in composite materials for construction. It has been adopted to characterize the bond in steel reinforced concrete [17–20], concrete reinforced by fiber reinforced polymer (FRP) bars [21–25], textile reinforced concrete [26,27] as well as natural fiber reinforced concrete [15]. In the case of strengthening/retrofitting of existing structures, the test method is also referred to as the lap pull-out test [28] or the lap shear test [29–34]. The influences of different test setups on the bond properties were studied in [35].

In those tests, if the reinforcement is bonded externally to the matrix, the surface strains can be measured [36] using, e.g., the digital image correlation technique as documented in Refs. [35,37,38]. Taking the externally bonded FRP sheet as an example, if its strain profile is known then the shear stress in the bond interface can be determined using a difference formula, and the corresponding slip can be found by a numerical integration of the measured axial strains [39]. However, when the reinforcement is embedded inside the matrix as in the pull-out tests of TRC, it is generally not possible to measure a bond-slip law directly due to the lack of straightforward and precise measuring techniques for the strain field along the reinforcement within the embedded length.

A variety of calibration methods have been developed to identify the constitutive laws that cannot be directly measured in experiments. These methods can be classified into two categories: those using optimization algorithms to minimize the lack of fit between the experimental result and the numerical simulation [15,22,23,26,40–44]; and those giving analytical or semi-analytical solutions [19,28,45,46]. The procedures employing optimization algorithms, while being more intuitive and easier to formulate, are usually computationally expensive and allow only a limited number of free parameters in the assumed constitutive models. Moreover, convergence of the optimization algorithms and uniqueness of the solutions cannot be guaranteed [42]. On the other hand, the analytical solutions are more difficult to derive and less flexible compared to the methods in the first category. Such solutions are only applicable to the given boundary conditions and to the particular form of constitutive law.

In the present paper, we propose a novel method of inverse analysis

* Corresponding author.
E-mail address: liyingxiong@live.com (Y. Li).

https://doi.org/10.1016/j.compositesb.2017.11.014
Received 11 April 2017; Received in revised form 19 September 2017; Accepted 2 November 2017
Available online 06 November 2017

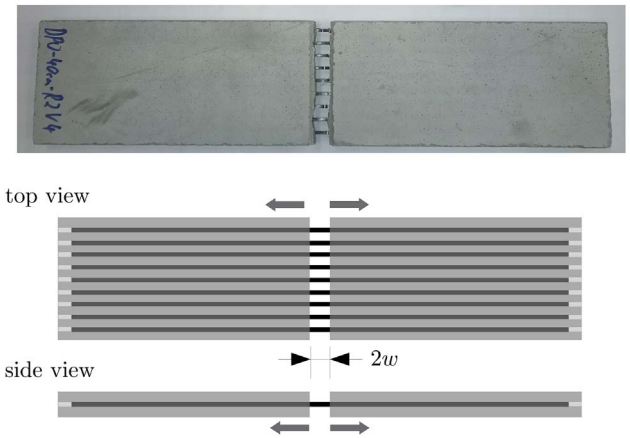

Fig. 1. Schematic diagram of a double-sided pull-out specimen with the pre-defined crack at the center, w is the pull-out displacement from each side.

to identify a multilinear bond-slip law based on a finite element formulation of the pull-out problem. We describe the applied method of implementing the procedure using modern, open-source utilities for scientific computing and provide the executable code. At the same time, we present an example of a calibration and validation procedure utilizing a recently developed test setup shown in Fig. 1. The motivation for development of this symmetric, double-sided pullout-test was to appropriately reflect the condition of a typical crack bridge as it occurs in structural TRC members under tensional or bending loads.

2. The direct and inverse pull-out problems

The idealized geometry and boundary conditions of a pull-out test are shown in Fig. 2. The measured output of such a test is typically provided as the relationship between the pull-out force P and the displacement w. Two related problems can be formulated based on the pull-out test, the direct pull-out problem and the inverse pull-out problem. The direct pull-out problem provides a prediction of the experimental results in terms of the pull-out force vs. displacement curve for a given bond-slip law. The inverse pull-out problem is used to determine the unknown bond-slip law given an experimentally measured force-displacement pull-out curve.

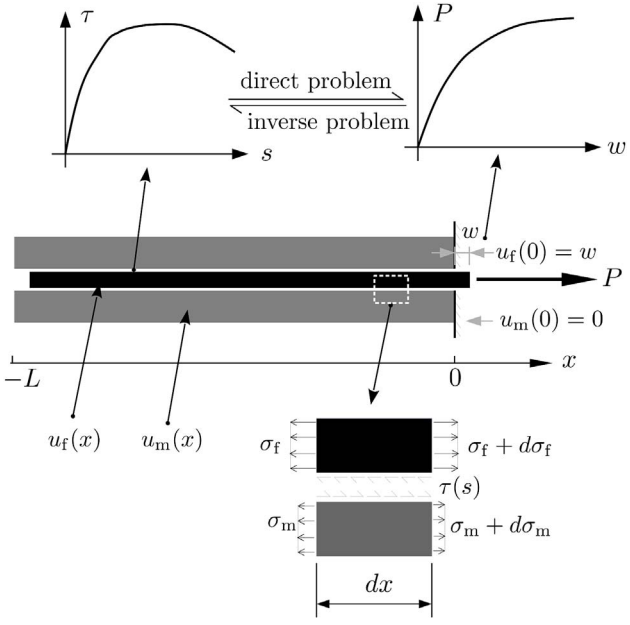

Fig. 2. A mechanical model of the pull-out problem.

The mathematical idealization of the direct pull-out is formulated as an initial boundary value problem reflecting equilibrium and compatibility conditions, as well as the material behavior of bond, matrix and reinforcement. In the considered case of cementitious composites with a negligible shear deformation the problem can be regarded as one-dimensional. The bond between the reinforcement and the matrix is assumed in form of a general nonlinear function $\tau(s)$ coupling the shear stress τ with the slip s.

With the described assumptions, the equilibrium condition of an infinitesimal segment of the reinforcement shown in Fig. 2 can be expressed as

$$A_f \sigma_{f,x} - p\tau(s) = 0, \tag{1}$$

where the index $(.)_{,x}$ denotes the derivative with respect to the spatial coordinate x. The cross-sectional area and the perimeter of the reinforcement are denoted as A_f and p, respectively. Similarly, the equilibrium of the matrix can be expressed as

$$A_m \sigma_{m,x} + p\tau(s) = 0, \tag{2}$$

where A_m is the cross-sectional area of the matrix.

The slip in the bond interface is defined as

$$s = u_f - u_m, \tag{3}$$

where u_f and u_m denote the reinforcement displacement and matrix displacement, respectively. The second derivative of s reads

$$s_{,xx} = \varepsilon_{f,x} - \varepsilon_{m,x}, \tag{4}$$

where ε_f is the reinforcement strain and ε_m is the matrix strain. The constitutive laws of the reinforcement and the matrix are given as

$$\sigma_f = D_f(\varepsilon_f),\ \sigma_m = D_m(\varepsilon_m), \tag{5}$$

which in combination with Eqs. (1) and (2) leads to

$$\varepsilon_{f,x} = \frac{1}{A_f}\frac{\partial C_f}{\partial \sigma_f} p\tau(s),\ \varepsilon_{m,x} = -\frac{1}{A_m}\frac{\partial C_m}{\partial \sigma_m} p\tau(s), \tag{6}$$

with the material compliances of the matrix and reinforcement given as $C_{(.)} = D_{(.)}^{-1}$. Substituting Eq. (6) into Eq. (4) the following second order differential equation is obtained,

$$s_{,xx} = \left[\frac{1}{A_f}\frac{\partial C_f}{\partial \sigma_f} + \frac{1}{A_m}\frac{\partial C_m}{\partial \sigma_m}\right] p\tau(s). \tag{7}$$

Thus, the direct pull-out problem shown in Fig. 2 involves the solution of the following boundary value problem for a given bond-slip law $\tau(s)$,

$$\begin{aligned} s_{,xx} &= \gamma p\tau(s), \\ s_{,x}(-L) &= 0, \\ s(0) &= w, \end{aligned} \tag{8}$$

where

$$\gamma = \frac{1}{A_f}\frac{\partial C_f}{\partial \sigma_f} + \frac{1}{A_m}\frac{\partial C_m}{\partial \sigma_m}. \tag{9}$$

Here w represents the control displacement of the reinforcement at the end being pulled out. For special types of the bond-slip law, analytical solutions of the problem are available [45–49]. For more general cases, numerical procedures such as the finite difference method or the finite element method can be employed. With the solution $s(x)$ for a given displacement w at hand, the corresponding pull-out force P can be obtained as an integral of the shear stress along the interface,

$$P(w) = \int_{-L}^{0} \tau(s(x; w))dx. \tag{10}$$

The pull-out response $P(w)$ is determined by solving Eq. (8) repeatedly for an increasing control displacement w and then evaluating the corresponding pull-out force P according to Eq. (10).

The aim of the inverse pull-out problem is in turn to identify a bond-slip law $\tau(s)$ that reproduces the experimentally measured pull-out

curve $P^E(w)$. The conventional approach is to predefine a bond-slip law containing several free parameters, thus the solution of the direct problem can be expressed explicitly or implicitly in terms of those free parameters. Then the free parameters can be identified by fitting the solution of the direct problem to the experimentally obtained pull-out curves. As mentioned in the introductory section, these approaches are computationally expensive and may exhibit convergence problems.

An interesting approach to the inverse analysis has been proposed in Ref. [19] in connection with an analytical pull-out problem formulation. It exploits the fact that the maximum slip occurs at the material point $x = 0$ in the bond interface and, thus, one can focus on this single point rather than the whole bond interface. In addition, a general bond-slip law is represented by a piecewise linear function and, thus, the solution space is not limited to a specific form of a bond-slip law. This concept is used and extended here to provide a numerical tool for inverse analysis of the pull-out problem.

3. Numerical model of the direct pull-out problem

3.1. Variational formulation

In order to provide a more general model of the pull-out problem defined by the differential Eqs. (1) and (2), we reformulate the boundary value problem in a weak form within the domain $\Omega:=[-L, 0]$ shown in Fig. 2. The essential and natural boundary conditions are specified as

$$\begin{aligned} &u_\mathrm{m} = \bar{u}_\mathrm{m}(\theta) \text{ on } \Gamma_{u_\mathrm{m}},\ \sigma_\mathrm{m} A_\mathrm{m} = \bar{t}_\mathrm{m}(\theta) \text{ on } \Gamma_{t_\mathrm{m}},\\ &u_\mathrm{f} = \bar{u}_\mathrm{f}(\theta) \text{ on } \Gamma_{u_\mathrm{f}},\ \sigma_\mathrm{f} A_\mathrm{f} = \bar{t}_\mathrm{f}(\theta) \text{ on } \Gamma_{t_\mathrm{f}}, \end{aligned} \tag{11}$$

in which Γ_{u_m}, Γ_{t_m}, Γ_{u_f} and Γ_{t_f} denote the boundary points where the corresponding boundary conditions are applied. The essential boundary conditions $\bar{u}_\mathrm{mf}$ and the natural boundary conditions $\bar{t}_\mathrm{mf}$ are prescribed as functions of the intrinsic time variable θ which is used to control the loading history. Denoting the integration of the product of two functions u, v over the domain V as $(u, v)_V$, the weak formulation can be expressed as

$$\begin{aligned} &(\delta u_\mathrm{m}, A_\mathrm{m}\sigma_{\mathrm{m},x} + p\tau)_\Omega &&+ (\delta u_\mathrm{f}, A_\mathrm{f}\sigma_{\mathrm{f},x} - p\tau)_\Omega +\\ &(\delta u_\mathrm{m}, -A_\mathrm{m}\sigma_\mathrm{m} + \bar{t}_\mathrm{m}(\theta))_{\Gamma_{t_m}} &&+ (\delta u_\mathrm{f}, -A_\mathrm{f}\sigma_\mathrm{f} + \bar{t}_\mathrm{f}(\theta))_{\Gamma_{t_f}} +\\ &(\delta u_\mathrm{m}, u_\mathrm{m} - \bar{u}_\mathrm{m}(\theta))_{\Gamma_{u_\mathrm{m}}} &&+ (\delta u_\mathrm{f}, u_\mathrm{f} - \bar{u}_\mathrm{f}(\theta))_{\Gamma_{u_f}} = 0. \end{aligned} \tag{12}$$

Here δu_m and δu_f denote the test functions that are assumed to have continuous first derivatives, are L^2 integrable and to implicitly fulfill the essential boundary conditions (see e.g. Ref. [50]). Since $\delta u_\mathrm{m} = 0$ on Γ_{u_m} and $\delta u_\mathrm{f} = 0$ on Γ_{u_f}, the last two terms in Eq. (12) vanish. Using integration by parts, the orders of the stress derivatives $\sigma_{\mathrm{m},x}$ and $\sigma_{\mathrm{f},x}$ in the above integration can be reduced as follows

$$(\delta u_{(.)}, A_{(.)}\sigma_{(.),x})_\Omega = (\delta u_{(.)}, A_{(.)}\sigma_{(.)})_\Gamma - (\delta u_{(.),x}, A_{(.)}\sigma_{(.)})_\Omega \tag{13}$$

Then, by substituting Eq. (13) for both matrix and reinforcement into Eq. (12), the following variational formulation of the pull-out problem is obtained

$$\begin{aligned} &(\delta u_{\mathrm{m},x}, A_\mathrm{m}\sigma_\mathrm{m})_\Omega &&+ (\delta u_\mathrm{f} - \delta u_\mathrm{m}, p\tau)_\Omega &&+\\ &(\delta u_{\mathrm{f},x}, A_\mathrm{f}\sigma_\mathrm{f})_\Omega &&- (\delta u_\mathrm{m}, \bar{t}_\mathrm{m}(\theta))_{\Gamma_{t\mathrm{m}}} &&-\\ &(\delta u_\mathrm{f}, \bar{t}_\mathrm{f}(\theta))_{\Gamma_{t\mathrm{f}}} &&= 0. \end{aligned} \tag{14}$$

The obtained functional is prepared for discretization using the finite element method. By choosing linear shape functions to approximate the displacement fields u_m and u_f and the test functions δu_m and δu_f we obtain the known finite element models of a pull-out problem, e.g. Refs. [51–53]. Higher-order shape functions with corresponding integration schemes can used be to generate advanced models of the pull-out problem.

In order to fully exploit the generic nature of the formulated functional we applied a novel approach to implementation of the finite element code. In particular, we used the index notation and the Einstein summation convention to obtain a compact form of the system equations that can be directly translated to an executable code. Similar approaches have been reported recently by other researchers, e.g., in Refs. [54,55]. A thorough description of the code for the direct pull-out problem is not the primary focus of the present paper. However, to make the paper self-contained and to demonstrate the advantages of the coding approach we provide its detailed description including a link to the code in Appendix A.

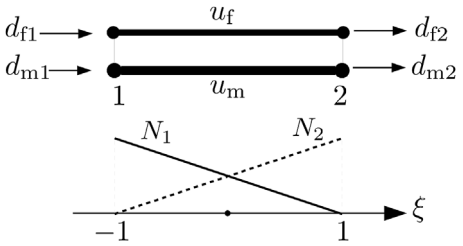

Fig. 3. Linear finite element with two displacement fields.

3.2. Finite element implementation

For the current study, we use the finite element model proposed by Herrmann [52], which was proved to be efficient for the direct pull-out problem [56,57]. The two-node element shown in Fig. 3 uses the linear shape functions

$$N_1 = (1 - \xi)/2,\ \ N_2 = (1 + \xi)/2 \tag{15}$$

for both displacement fields and two integration sampling points at

$$\xi_1 = -1,\ \xi_2 = 1, \tag{16}$$

with the corresponding weights given as

$$w_1 = w_2 = 1. \tag{17}$$

By substituting these element parameters into the generic implementation described in Appendix A, we obtain the executable code of the direct pull-out problem.

The essential boundary conditions displayed in Fig. 2 read

$$\begin{aligned} &u_\mathrm{m} = 0 \text{ on } x = 0,\\ &u_\mathrm{f} = w \text{ on } x = 0. \end{aligned} \tag{18}$$

The pull-out force P, expressed as an implicit function of the displacement w and bond-slip law $\tau(s)$

$$P = P(\tau(s), w) \tag{19}$$

are then numerically evaluated using Eq. (A.17). The above equation forms the basis for solving the inverse pull-out problem.

4. Sequential inverse analysis of the pull-out problem

With the efficient solver for the direct pull-out problem at hand, we can implement a calibration framework for a general pull-out test. It is applicable in combination with linear as well as nonlinear material behavior of the matrix and reinforcement. At the same time, it can be embedded in a two- or three dimensional discretization of the matrix.

4.1. Description of the algorithm

The calibration is formulated for generally shaped piecewise linear bond-slip laws. It exploits three properties of a pull-out boundary value problem (see Figs. 2 and 5):

- the maximum slip occurs at the position $x = 0$,
- the slip at the position $x = 0$ equals the pull-out control displacement, i.e. $s(x = 0) = w$, and

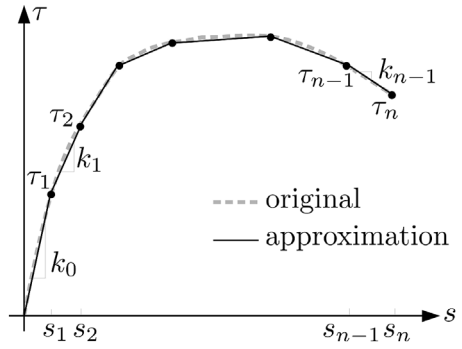

Fig. 4. Bond-slip law approximated with a multilinear function.

- at any other point within the embedded length $-L \le x < 0$, the slip $s(x) < w$.

Based on these observations, we can conclude that all values of slip less than the current control displacement ($s \le w$) must have occurred during the loading history at some lower level of loading at the position $x = 0$. As a consequence, the shear stress for any lower value of slip than the current control displacement can be assumed as already known.

In order to introduce the incremental formulation of the calibration procedure, we assume that the bond-slip curve is known for all steps $j = 0...i-1$ with the value pairs (τ_j, s_j) corresponding to a piecewise linear function (Fig. 4)

$$\tau(s) = \tau_j + k_j(s - s_j), \tag{20}$$

where

$$s_j < s \le s_{j+1}, \;\; s_0 = \tau_0 = 0$$

$$k_j = (\tau_{j+1} - \tau_j)/(s_{j+1} - s_j).$$

Now, for the next value of slip $s_i > s_{i-1}$ we seek the new value of τ_i that would satisfy the equilibrium condition given in Eq. (19), such that

$$P(\tau_i; w_i) = P^E(w_i), \;\; w_i = s_i \tag{21}$$

where $P^E(w_i)$ represents the pull-out force measured experimentally at the control displacement w_i. The root finding algorithm, such as the Brents method [58] can be used effectively for the solution of Eq. (21) such that the unknown shear stress τ_i is determined.

Fig. 5 shows the quantitative correspondence between three chosen values of τ_i (Fig. 5b) and the corresponding pullout forces P (Fig. 5d) satisfying the equilibrium condition Eq. (19). Apparently, a small change of the pull-out force requires a large change of the value of τ_i. This sensitivity is natural due to the fact that the pull-out force P is evaluated as an integral of shear stress in the interface (Eq. (10)), thus it equals to the area below the shear stress profile shown in Fig. 5a. The value of τ_i influences only a rather small part of the area (the right part, shaded in lighter gray). This property reveals the sensitivity of the calibration procedure with respect to small perturbations in the measured experimental response, which shall be discussed in detail in the remainder of this section.

4.2. Verification for elementary use cases

To verify the proposed inverse analysis procedure, we check whether or not it is able to reproduce an *a-priori* given bond-slip law. We consider three types of a given bond-slip law $\tau(s)$ with analytically or numerically calculated pull-out response curves $P(w)$. Then, we test the ability of the proposed inverse analysis to reproduce the original bond-slip laws.

In the first case (a), the linear bond-slip law is given as $\tau = 2s$, shown as the solid line in the bottom diagram of Fig. 6a. The input data shown in the top diagram of Fig. 6a is the analytically obtained pull-out response curve, using the solution [45].

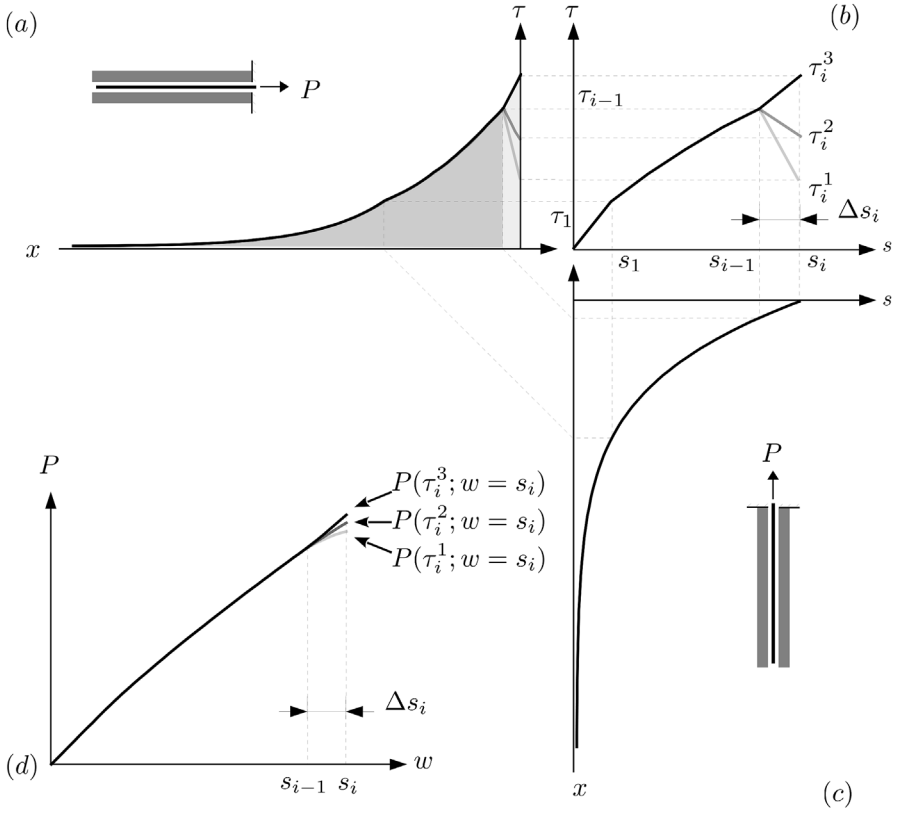

Fig. 5. Solution step i of the inverse pull-out problem: (a) the shear stress profile in the interface; (b) the bond-slip law for an intermediate state with three possible values of τ_i; (c) the slip profile in the interface; (d) numerically evaluated pull-out curves.

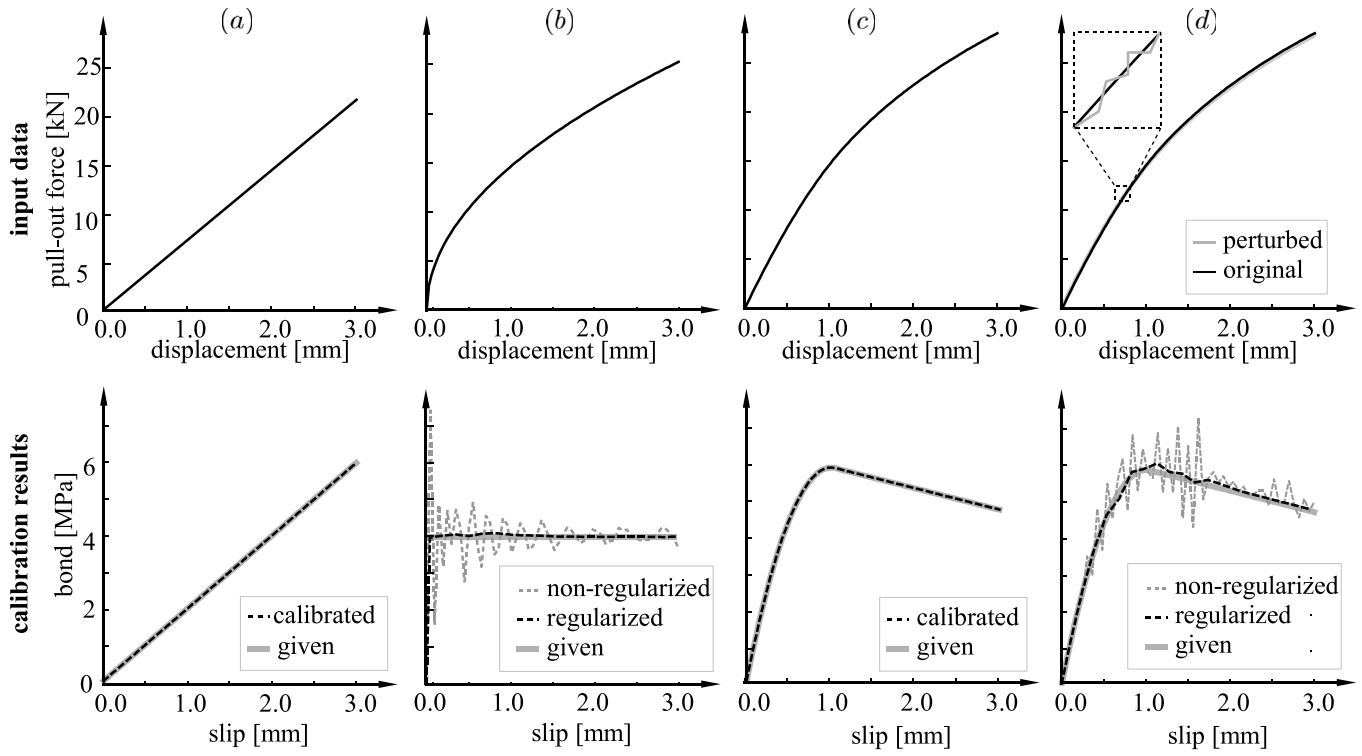

Fig. 6. Verification examples: (a) constant bond; (b) linear bond-slip law; (c) nonlinear bond-slip law; (d) nonlinear bond-slip law and perturbed pull-out response curve.

$$P(w) = \frac{k\tanh(\alpha L)}{\alpha} w, \tag{22}$$

in which k is the slope of the linear bond-slip law, L is the embedded length, and the coefficient α can be written as

$$\alpha = \sqrt{pk\left(\frac{1}{E_f A_f} + \frac{1}{E_m A_m}\right)}, \tag{23}$$

where p denotes the perimeter of the interface. The other geometrical and material parameters of the pull-out problem are summarized in Table 1. The result of the sequential inverse analysis reproduces the prescribed bond-slip law exactly as documented by the dashed line in the bottom diagram of Fig. 6a.

In the second case (b), a constant bond-slip law is prescribed as $\tau = 4$ (Fig. 6b, bottom) and the analytical solution with infinite embedded length [59].

$$P(w) = \sqrt{2wp\tau \frac{E_f A_f E_m A_m}{E_f A_f + E_m A_m}} \tag{24}$$

is used as the input data. Apparently, the calibrated bond-slip law (gray dashed line) exhibits oscillations. This is due to the fact that the calibrated bond-slip law implicitly starts at the point $\tau(0) = 0$ (Fig. 5b) and, thus, cannot exactly reproduce the constant curve starting at $\tau(0) = 4$. This example indicates that the calibration might be sensitive to non-smooth data obtained from the experimental measurement, an issue that deserves attention as we discuss later on.

In the third case (c), a general, nonlinear bond-slip law is assumed (Fig. 6c, bottom), for which no analytical solution exists. In particular, the used bond-slip law is given as

$$\tau = \begin{cases} -6s^2 + 12s, & 0 \le s \le 1.05 \\ -0.6s + 6.615, & 1.05 < s \le 3. \end{cases} \tag{25}$$

The corresponding pull-out curve is calculated using the direct pull-out problem solver described in Eq. (19) and serves as synthetic input data for the inverse analysis. The calibrated bond-slip law fits exactly the given curve.

Based on these verification tests, the calibration procedure seems to be well suited for processing the general pull-out test results. However, regarding the oscillations observed in Fig. 6b we need to consider the fact that experimentally measured data is not perfectly smooth. Thus it is worth examining the sensitivity of the algorithm with respect to perturbed input data.

In Fig. 6d, the pull-out curve from Fig. 6c is artificially perturbed and the calibration of the bond-slip law is repeated. The result shown as the gray dashed line in the corresponding bottom diagram

Table 1
Parameters used in the verification examples.

case#	(a)	(b)	(c)	(d)
matrix area [mm^2]	1543.35	1543.35	1543.35	1543.35
matrix modulus [MPa]	28484	28484	28484	28484
reinforcement area [mm^2]	16.65	16.65	16.65	16.65
reinforcement modulus [MPa]	170000	170000	170000	170000
bond interface perimeter [mm]	10	10	10	10
specimen length [mm]	2000	infinite	700	700
bond-slip law type	linear	constant	nonlinear	nonlinear
input data	analytical solution	analytical solution	synthetic data	perturbed data

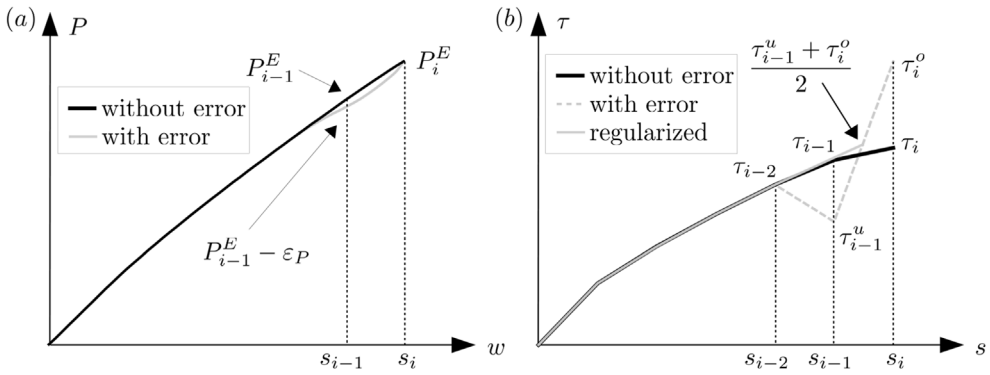

Fig. 7. Averaging procedure: (a) experimental pull-out force with and without error at the step $i-1$; (b) the calibrated bond-slip law.

demonstrates that the introduced perturbations result in large oscillations of the obtained bond-slip law. This reveals the well known ill-posed nature of the inverse problems as summarized in Ref. [60]. In order to deal with this problem, two approaches are possible:

- smooth the experimental data using regression techniques,
- regularize the calibrated bond-slip law *on-the-fly*.

The smoothing techniques are easy to implement, however they cannot handle the problem observed in Fig. 6b. The deviation of the calibrated bond value at one point ($s = 0$) propagates to further steps, causing oscillation of the calibrated law within a wide range. Hence, we propose to include the *on-the-fly* regularization technique within the sequential calibration procedure.

4.3. Regularization technique

In order to regularize the calibration, let us first take a closer look at the reason for the oscillations. Suppose that at the step $i-1$ there is an error ε_P in the experimental pull-out force $P^E(w = s_{i-1})$ (the gray line in Fig. 7a) leading to an underestimated bond value $\tilde{\tau}_{i-1}$ as shown in Fig. 7b. At the next step, the algorithm delivers an overestimated value $\tilde{\tau}_i$ as a compensation in order to reproduce the same pull-out force $P^E(w = s_i)$. This explains the oscillations observed in Fig. 6b and Fig. 6d.

The regularization technique exploits the fact that the overestimation of τ_i at one step leads to the underestimation at the next step, and vice versa. Considering two points $[s_{i-1}, \tilde{\tau}_{i-1}]$ and $[s_i, \tilde{\tau}_i]$ we calculate their average $[\bar{s} = (s_{i-1} + s_i)/2,\ \bar{\tau} = (\tilde{\tau}_{i-1} + \tilde{\tau}_i)/2]$ as shown in Fig. 7b. The obtained bond-slip law (the gray solid line) is close to that derived from the experimental data without any error (the black solid line). The averaged data point is directly used in the next load increment so that we refer to this type of regularization as *on-the-fly* averaging.

In a general case, the regularization involves R data points in each step. Assuming that the in the averaged bond-slip law will conssit of K value pairs $[\bar{s}_k, \bar{\tau}_k],\ k \in (1, K)$, each of which is averaged using R calculated data points, we can write the general averaging formula as

$$\bar{s}_k = \frac{1}{R}\sum_{i=(k-1)R+1}^{kR} s_i,\ \bar{\tau}_k = \frac{1}{R}\sum_{i=(k-1)R+1}^{kR} \tilde{\tau}_i. \tag{26}$$

The averaged values $[\bar{s}_k, \bar{\tau}_k]$ are used in the subsequent calculation step $k+1$ of the pull-out force. In other words, the incremental calibration of the bond-slip law incorporates the averaged values right after every R steps. Let us remark, that this kind of interleaved, *on-the-fly* averaging is essencial for a robust calibration procedure that is insensitive to data perturbations.

The proposed technique has been verified using the cases (b) and (d) in Fig. 6. As shown by the black dashed lines in Fig. 6b and Fig. 6d, the oscillations are drastically reduced and the regularized results are close to the given bond-slip laws. In general, the more severe the oscillations are, the larger the value of R should be. The regularized bond-slip laws for the cases (b) and (d) are obtained with $R = 2$ and $R = 4$, respectively.

5. Application to calibration of the bond-slip law in TRC

Driven by the need for an approach to test textile reinforcement with low bond stress and long anchorage characteristics, a novel test setup with hydraulic clamping to investigate the behavior of TRC under uniaxial tensile loading has been recently developed at the Institute for Structural Concrete, RWTH Aachen University [61]. Using a similar test setup, double-sided pull-out tests of thin TRC specimens with styrene-butadiene impregnated carbon textile reinforcement have been carried out.

In the test setup shown in Fig. 8, a TRC specimen with a notch on both faces at the middle section is clamped using hydraulic cylinders. The proposed test setup induces high transversal stress into the anchorage zone of the specimen. For non-impregnated yarns and yarns with a flexible impregnation, e.g. styrene-butadiene, the bond characteristics are not influenced by transversal pressure if the concrete remains uncracked in longitudinal direction. This effect was studied by utilizing specimens where the steel plates were adhesively bonded instead of hydraulically clamped. There, no difference between the pull-out behavior of the clamped and the adhesively fixed specimens was observed. Due to the low stiffness of the yarns in comparison to the concrete in transversal direction, the transversal pressure is transferred by small concrete vaults, forming around the yarn channels (Fig. 8c). The horizontal force components resulting from the vault action were low and did not lead to formation of longitudinal cracks in the clamping zone.

The cross section of the specimens has the dimensions of 120 × 13 mm^2, the specimen length was chosen as an experimental parameter ranging from 200 mm to 700 mm. The specimens were cut from one large TRC plate, which guaranteed the homogeneity of the material properties of all specimens and avoided the influence of boundary effects. In total, 15 specimens were produced. Table 2 summarizes the number of the specimens for each tested length. At the beginning of the test a crack through the full cross-section in the matrix was provoked at the position of the notch. The reinforcement was then pulled out from both sides during the loading process.

The material behavior of the matrix and reinforcement was assumed linear-elastic. In each specimen there were 9 parallel 3300 tex yarns with the cross-sectional area of 1.85 mm^2 in the loading direction, the Youngs modulus of the yarns was determined as high as 170 GPa using the single yarn tensile test. The applied fine-grained concrete had Youngs modulus of 28.48 GPa. The relevant material and geometrical parameters are summarized in Table 3.

Fig. 9 shows the results of the double-sided pull-out tests, i.e., the relationship between the pull-out force and the crack opening at the middle. Fig. 10 shows the final failure modes of one representative specimen for each length. From Fig. 9 one can observe that the pull-out

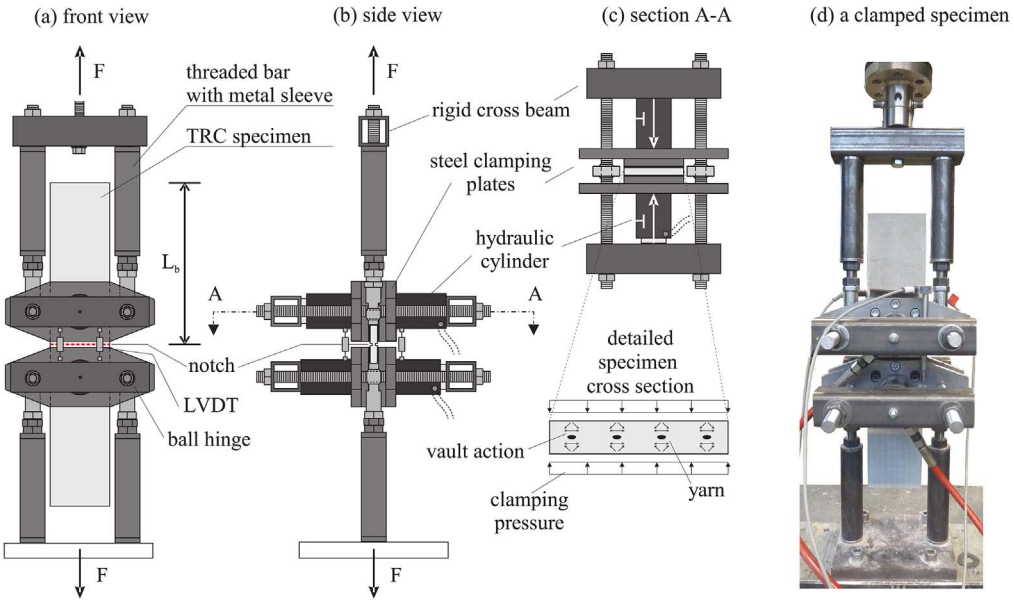

Fig. 8. Test setup for double-sided pull-out tests: (a) front view; (b) side view; (c) cross section; (d) a clamped specimen.

Table 2
Number of specimens tested for each length.

Length [mm]	200	300	400	500	600	700
Amount	2	3	3	2	3	2

Table 3
The measured geometrical and material parameters.

matrix area [mm^2]	1543.35
matrix stiffness [GPa]	28.48
reinforcement area [mm^2]	16.65
reinforcement stiffness [GPa]	170
specimen length [mm]	200–700

curves generally consist of three branches, and the achieved maximum pull-out force in the first branch increases monotonically with the specimen length. It is important to note that the peak at the end of the first branch of the pull-out curve is induced by the bond-slip interaction between the penetrated yarn and the matrix and does not represent an initiation of the matrix crack within the notched section. Indeed, the cracking of the remaining matrix section at the notch occurred at lower levels of tensile loading (2–3 kN). The event of emerging matrix crack has been subtracted from the pull-out response as it has no effect on the measured bond behavior and should not enter the calibration of the bond-slip law.

As shown in Fig. 10, the failure of the shorter specimens was caused by the pull-out of the yarns. In case of longer specimens, the failure was initiated by the rupture of one of the yarns. This explains the sudden drop of the pull-out forces observed in the latter parts of the pull-out curves for the longer specimens. For the 70 cm specimens, a virtually brittle failure mode was observed.

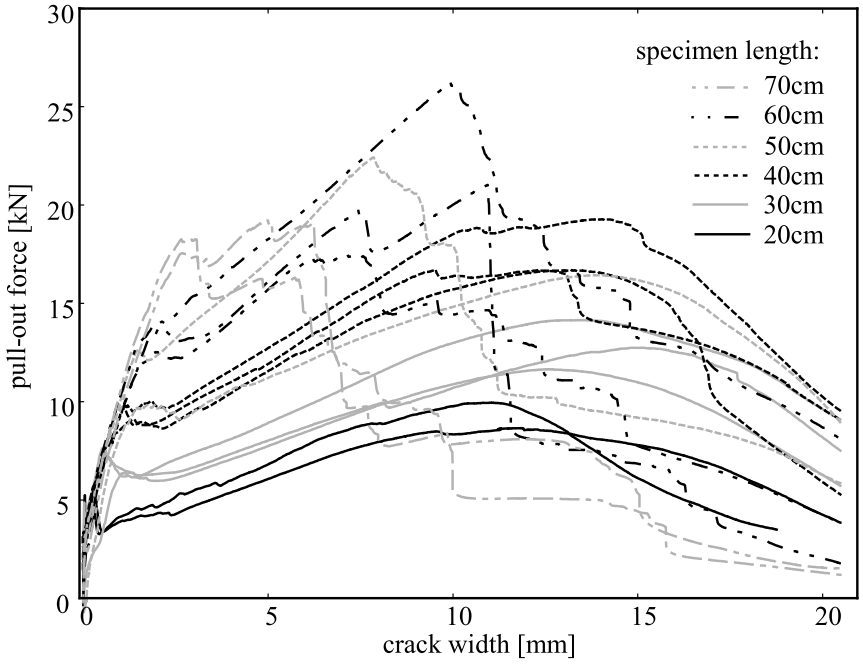

Fig. 9. Crack opening vs. pull-out force curves.

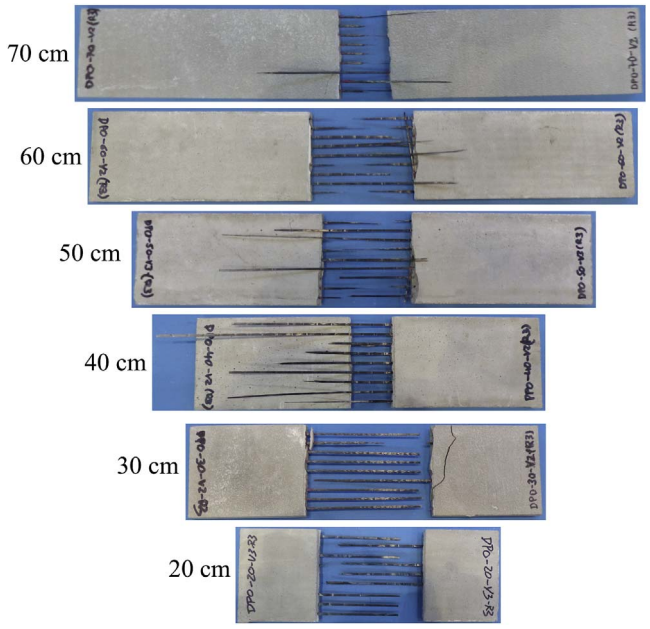

Fig. 10. Examples of specimens showing the amount of pulled-out and ruptured yarns.

The failure of parallel multiple yarn systems represents a rather complex phenomena [62] that can be addressed using a stochastic treatment. However, this issue goes beyond the scope of the current paper. In the tests of shorter specimens (20 cm, 30 cm and 40 cm), yarn rupture was not observed before the peak load. Furthermore, after the peak load, the assumed symmetric double-sided pull-out condition is no longer provided. Each yarn is pulled-out only from the side with slightly weaker bond properties (see e.g. the 30 cm specimen in Fig. 10).

In order to determine the bond-slip law, we used only the ascending branches of the measured response for which the symmetry of the underlying double-sided pullout boundary value problem can be assumed. Then, we can set the half of the measured crack opening equal to the pull-out displacement on each side (Fig. 1). As has been pointed out in Ref. [47], the cross section of an embedded yarn is not always of regular circular shape, so it is difficult to determine the perimeter of the bond interface. Hence, we normalized the bond intensity to shear force per yarn per unit length.

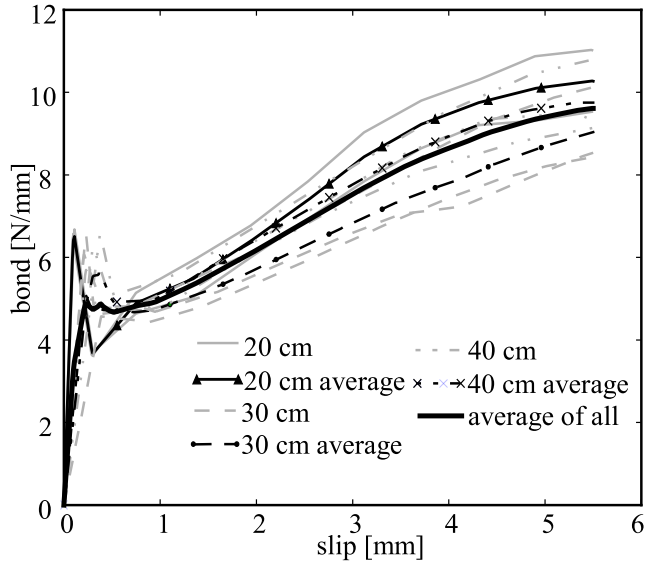

Fig. 11. The calibrated bond-slip laws based on test results of 20 cm, 30 cm and 40 cm specimens.

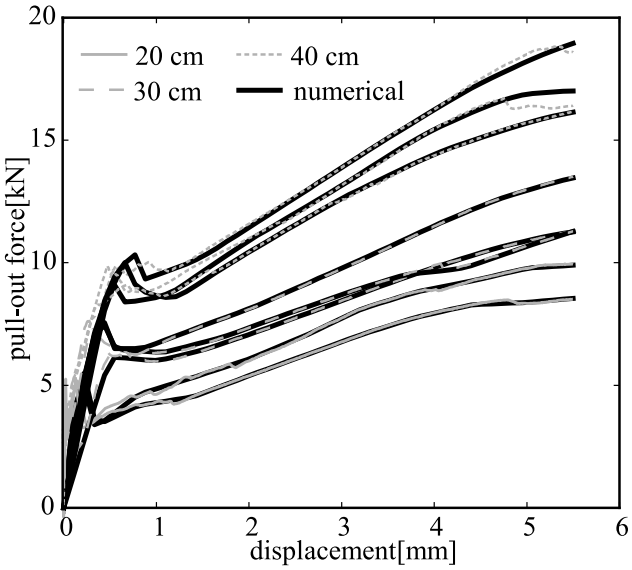

Fig. 12. Verification of the calibration procedure: comparison of the numerically reproduced pull-out curves with the original experimental curves.

Fig. 11 shows the calibrated bond-slip law obtained with the test results of 20 cm, 30 cm and 40 cm specimens, the gray lines show the bond-slip laws derived from the test results of each individual specimen, the black lines show the averages. It can be observed that the bond-slip law is independent of the specimen length. Fig. 12 compares the numerically reproduced pull-out curves using the calibrated bond-slip law with the experimental ones. This study only verifies that the pull-out curves used for calibration are reproduced with the calibrated bond-slip laws.

The identified average bond-slip law has then been used to numerically predict the pull-out curves of the longer (50 cm, 60 cm and 70 cm) specimens as shown in Fig. 13. As yarn rupture has not been considered in the numerical model, the predicted pull-out force is larger than the experimental value at the latter stage of the test where yarn rupture occurs. Nevertheless, the initial parts of the predicted pull-out curves agree well with the experimental data, which demonstrates that the calibrated bond-slip law can well represent the mechanical behavior of the bond. The discrepancies at the latter stage were mainly caused by the yarn rupture. Fig. 12 and Fig. 13 validate that the proposed procedure can accurately identify the bond-slip law of the investigated TRC.

Interestingly enough, the identified bond-slip law exhibits slip-hardening behavior. A possible source of this unusual behavior can be sought in the applied penetration material, styrene-butadiene with a relatively low stiffness. A similar type of slip-hardening behavior has been observed in pull-out of PVA fibers from concrete [63] and explained by a jamming effect increasing the lateral pressure in the interface zone between the fiber and matrix.

6. Conclusions

The bond-slip law in the bond interface is an important material parameter for cementitious composites such as TRC. In this paper, we proposed a finite element method based procedure to solve the inverse pull-out problem, i.e., to identify the bond-slip law from the pull-out tests. The bond-slip law is represented as a multilinear function without any restriction on its shape.

Due to the fact that the pull-out force is evaluated as the integral of the shear flow in the bond interface, the inverse pull-out problem is inherently ill-posed and, therefore, delivers oscillating results. The

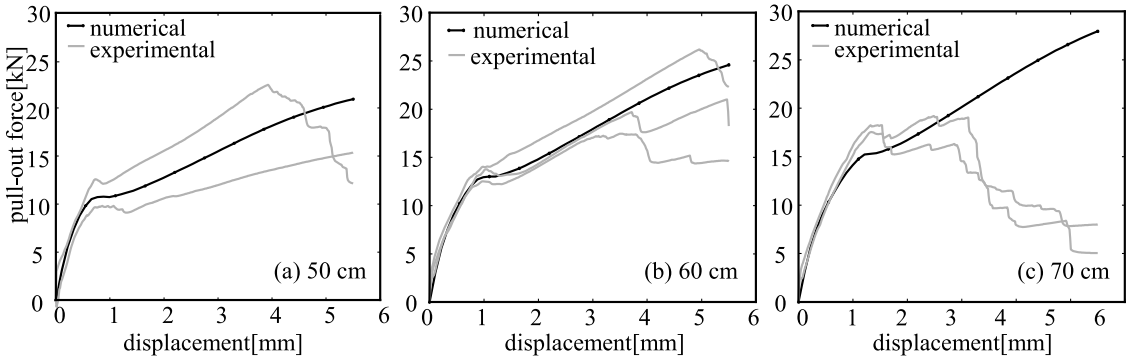

Fig. 13. Predicted pull-out curves for: (a) 50 cm specimen; (b) 60 cm specimen; (c) 70 cm specimen.

sources for the oscillations have been analyzed and a regularization technique has been proposed as a remedy.

The verification examples performed for elementary cases of bond-slip laws demonstrate the feasibility of the calibration procedure.

Double-sided pull-out tests with varied length of the TRC specimens were performed to obtain the data necessary for the validation of the bond characterization approach. It was possible to identify an objective bond-slip law that could reproduce the pull-out response for all tested specimen lengths. In other words, the obtained bond-slip law is independent of the specimen length, so that it can be regarded as a local material parameter.

Besides the formulation of the direct pull-out problem and inverse analysis procedure, we have described an novel approach to implementation of the finite element code utilizing the current open-source tools for scientific computing. However, the concept of inverse analysis is general and can be combined with standard finite element codes providing application-programming interfaces to control the sequence of analysis steps. In particular, finite element models focused on specific effects of the direct pull-out, reported e.g. in Refs. [64–69] can be readily included in the described approach to inverse analysis.

We remark that the proposed procedure is not limited to the calibration of bond-slip laws but can be easily extended to more general inverse problems. The described concept and the implementation of the inverse pull-out problem can be applied to two- or three-dimensional boundary value problems. An example of a similar inverse analysis is provided by the cohesive crack-opening law describing the strain-softening behavior within a fracture process zone in quasi-brittle materials.

Acknowledgements

This work was supported by the German Federal Ministry of Education and Research (BMBF) as part of the Carbon Concrete Composite (C^3) initiative, Project C^3-B3 and C^3-V1.2. This support is gratefully acknowledged.

Appendix A. Index-based finite element code

As mentioned in Sec. 3.2, we have implemented the direct pull-out problem using a novel approach exploiting the currently available open-source libraries for scientific computing. In order to make the paper self-contained and to share the concept with the broader scientific community, we briefly describe the implementation method here and provide the corresponding code in the open-source *github. com* repository [70]. The implementation approach utilizes two new features provided by current tools for scientific computing that have become available during the recent decade:

- multi-dimensional arrays, and
- highly efficient multi-dimensional index operators based on the Einstein summation rule.

In order to exploit these two concepts, we need to formulate the finite element model of the direct pull-out problem in index form. Then, it can be directly translated into an efficient, executable code that is conceptually identical with the underlying mathematical description. In this way, the implementation process becomes very straightforward and almost faultless. At the same time, we do not have to compromise efficiency in relation to the traditional, loop-based, compiled finite element implementations. Finally, the code is easily portable and installable on any platform.

Appendix A.1Index notation

To allow for the Einstein summation rule not only for spatial dimensions, nodes, elements and integration points, but also for individual material components, we replace the subscripts $(.)_{\mathrm{m}}$ and $(.)_{\mathrm{f}}$ with the indexes 1 and 2. In the present case of the pull-out problem, index 1 represents the matrix m and index 2 the reinforcement f. The convention implies summation over repeated indexes, for example the slip between the matrix and reinforcement given in Eq. (3) can be rewritten as

$$s = -u_{\mathrm{m}} + u_{\mathrm{f}} = (-1)^1 u_1 + (-1)^2 u_2 = (-1)^c u_c \tag{A.1}$$

with $c = 1,2$. To avoid ambiguity, we note that here the upper index c means both exponent and index, alternatively, $(-1)^c$ can be understood as the c-th component of the vector $\{-1,1\}$. Using this convention, the variational formulation in Eq. (14) can be rewritten as

$$(\delta u_{c,x}, F_c)_{\Omega} + (\delta u_c (-1)^c, p\tau)_{\Omega} - (\delta u_c, \bar{t}_c(\theta))_{\Gamma_{t_c}} = 0, \tag{A.2}$$

where F_c is the component of the vector $\{A_1\sigma_1, A_2\sigma_2\}$, and the term $\delta u_c(-1)^c = \delta(u_2 - u_1) = \delta s$ renders the virtual slip between the components.

Appendix A.2Finite element discretization

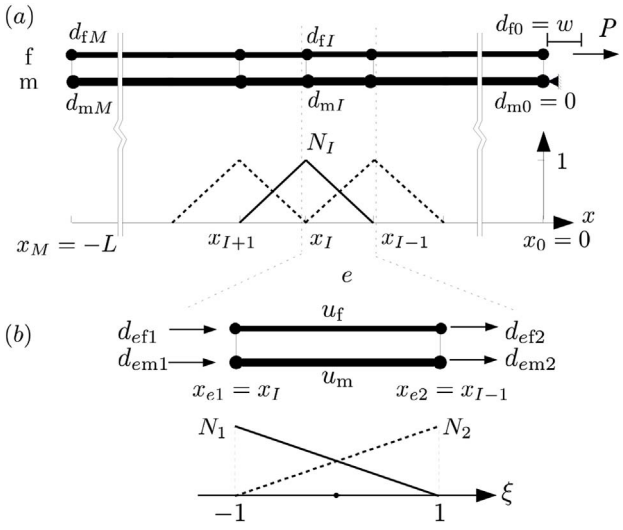

Fig. A.14. Index-based finite element discretization.

The displacement field of the material component c is approximated using the shape functions shown in Fig. A.14a,

$$u_c = N_I\, d_{cI},\ \ \delta u_c = N_I\, \delta d_{cI}$$

with the index $I = 1,2,\ ...,M$ representing the I-th node.

For brevity, we use globally defined shape functions, centered at the node I and covering two neighboring elements throughout this appendix. In the standard finite element implementation, an element-wise, parametric specification of the shape function is usual. The present mathematical expressions related to node I can be easily transformed into such kind of element-centered expressions using an index function $[e,\ i] \rightarrow I$ that defines the mapping of the local elemental degrees of freedom to the global nodal degrees of freedom (Fig. A.14b). This mapping function was used in the supplied code [70] to obtain an efficient, "loopless" assembly procedure of system matrix and force vectors.

The strain field and virtual strain field in each material component c are then expressed as

$$u_{c,x} = B_I\, d_{cI},\ \ \delta u_{c,x} = B_I\, \delta d_{cI} \tag{A.3}$$

where $B_I = N_{I,x}$, x is the global coordinate.[1] The slip field is approximated as

$$s = (-1)^c u_c = (-1)^c N_I d_{cI}, \tag{A.4}$$

so that, after substitutions, Eq. (A.2) reads

$$\delta d_{cI}(B_I,\ F_c)_\Omega + \delta d_{cI}((-1)^c N_I,\ p\tau)_\Omega - \delta d_{cI}(N_I,\ \bar{t}_c(\theta))_{\Gamma_{t_c}} = 0. \tag{A.5}$$

Since δd_{cI} is arbitrary, and $(N_I,\ \bar{t}_c(\theta))_{\Gamma_{t_c}}$ can be simplified to nodal loads as $\bar{t}_{cI}(\theta)$, Eq. (A.5) can be reduced to

$$R_{cI}^{(\theta)} = (B_I,\ F_c)_\Omega + ((-1)^c N_I,\ p\tau)_\Omega - \bar{t}_{cI}(\theta) = 0, \tag{A.6}$$

with $R_{cI}^{(\theta)}$ representing the residuum.

Appendix A.3Iterative solution algorithm

In case of nonlinear material behavior assumed either for the matrix, reinforcement or bond, Eq. (A.6) needs to be linearized using the Taylor expansion:

$$R_{cI}^{(\theta)}(d_{dJ}^{(k)}) \approx R_{cI}^{(\theta)}(d_{dJ}^{(k-1)}) + \left.\frac{\partial R_{cI}^{(\theta)}}{\partial d_{dJ}}\right|_{d_{dJ}^{(k-1)}} \Delta d_{dJ}^{(k)} = 0. \tag{A.7}$$

Since we do not consider geometrical nonlinearity and the nodal loads $\bar{t}_{cI}$ are assumed independent of the displacements, the derivative in Eq. (A.7) can be written as

$$\frac{\partial R_{cI}^{(\theta)}}{\partial d_{dJ}} = \left(B_I,\ \frac{\partial F_c}{\partial d_{dJ}}\right)_\Omega + \left((-1)^c N_I,\ p\frac{\partial \tau}{\partial d_{dJ}}\right)_\Omega. \tag{A.8}$$

In case of nonlinear material behavior of the components c, the derivative of the cross-sectional component force F_c with respect to d_{cI} reads

$$\frac{\partial F_c}{\partial d_{dJ}} = \frac{\partial F_c}{\partial \varepsilon_d}\frac{\partial \varepsilon_d}{\partial d_{dJ}} = \frac{\partial F_c}{\partial \varepsilon_d} B_J \tag{A.9}$$

Similarly, for nonlinear bond-slip law, the derivative of shear flow with respect to the nodal displacement can be written as

[1] The supplied code element-wise mapping also includes the usual geometry mappings of the local coordinate ξ (Fig. A.14b) and the global coordinate x using the Jacobian matrix.

$$\frac{\partial \tau}{\partial d_{dJ}} = \frac{\partial \tau}{\partial s}\frac{\partial s}{\partial d_{dJ}} = \frac{\partial \tau}{\partial s} N_J (-1)^d. \tag{A.10}$$

Thus, the tangential stiffness in Eq. (A.7) reads

$$\left.\frac{\partial R_{cI}^{(\theta)}}{\partial d_{dJ}}\right|_{d_{dJ}^{k-1}} = K_{cIdJ}^{(\theta,k-1)} = \left(B_I,\, B_J \left.\frac{\partial F_c}{\partial \varepsilon_d}\right|_{d_{dJ}^{k-1}}\right)_\Omega . + (-1)^{c+d} p \left(N_I,\, N_J \left.\frac{\partial \tau}{\partial s}\right|_{d_{dJ}^{k-1}}\right)_\Omega \tag{A.11}$$

The integrals in Eq. (A.11) are evaluated using the numerical quadrature,

$$(u,\, v)_\Omega = w_i X_i, \tag{A.12}$$

in which w_i is the weight factor and $X_i = u(\xi_i)v(\xi_i)$ the value of the product uv at the integration point ξ_i. Finally, by rewriting Eq. (A.7) the following incremental form of equilibrium is obtained

$$K_{cIdJ}^{(\theta,k-1)} \Delta d_{dJ}^{(k)} = -R_{cI}^{(\theta)}(d_{dJ}^{(k-1)}). \tag{A.13}$$

Appendix A.4Displacement control procedure

To introduce the boundary conditions $u_{\mathrm{m}}(x=0) = 0$ and $u_{\mathrm{f}}(x=0) = w$ we need to rearrange the system of nonlinear equilibrium conditions Eq. (A.6) into two parts [71]:

$$R_{cI_1}\left(\overline{d}_{c0},\, d_{cI_1}\right) = 0, \tag{A.14}$$

$$R_{c0}\left(\overline{d}_{c0},\, d_{cI_1}\right) = P_c \tag{A.15}$$

where $I_1 = 1...M$ counts the non-constrained nodes located within $\Omega - \Gamma_{u_c}$, i. e $-L \le x < 0$. The two equations indexed $c0 = [\mathrm{m0},\, \mathrm{f0}]$ represent the reaction forces at the constrained boundary $x = 0$. The iterative scheme for the direct pull-out displacement control is obtained by performing the linearization of the unconstrained residuum equation (A.14) and rewriting the iterative scheme given in Eq. (A.13) as

$$K_{cI_1dJ_1}^{(\theta,k-1)} \Delta d_{dJ_1}^{(k)} = -R_{cI_1}^{(\theta)}\left(d_{dJ_1}^{(k-1)}\right) - K_{cI_1d0}^{(\theta,k-1)} \Delta \overline{d}_{c0}^{(k)}. \tag{A.16}$$

This equation is solved iteratively until the convergence is reached. With the obtained nodal displacement vector d_{cI_1}, the pullout force can be evaluated by substituting it back to Eq. (A.15)

$$P = R_{\mathrm{f0}}\left(\overline{d}_{\mathrm{m0}} = 0,\, \overline{d}_{\mathrm{f0}} = w,\, d_{cI_1}\right). \tag{A.17}$$

Appendix A.5Implementation

To indicate how to transform the mathematical description into an executable code let us specify the code evaluating the first integral in the expression (A.6)

$$(B_I,\, F_c)_\Omega \tag{A.18}$$

using the numerical quadrature mentioned in Eq. (A.12) as

$$R_{cI}^{(1)} = w_i B_{Ii} F_{ci} \tag{A.19}$$

with automatic summation over the index i using the numpy. einsum method. Let us assume that w_i, B_{Ii} and F_{ci} are available as multidimensional numpy arrays w_i, B_Ii and F_ci, respectively. Then, resulting residual force in every node and material component of the finite element discretization is evaluated using the code

```
                import numpy as np                  1
R1  cI = np.einsum('i,li,ci->cl',w_i,B_li,F_ci)     2
```

Detailed description of the mapping between the mathematical formulation and the code is available in Ref. [70].

References

[1] Scholzen A, Chudoba R, Hegger J. Thin-walled shell structures made of textile-reinforced concrete. Struct Concr 2015;16(1):106–14.
[2] Sharei E, Scholzen A, Hegger J, Chudoba R. Structural behavior of a lightweight, textile-reinforced concrete barrel vault shell. Compos Struct 2017;171:505–14.
[3] Häußler-Combe U, Hartig J. Bond and failure mechanisms of textile reinforced concrete (trc) under uniaxial tensile loading. Cem Concr Compos 2007;29(4):279–89.
[4] Hartig J, Häußler-Combe U, Schicktanz K. Influence of bond properties on the tensile behaviour of textile reinforced concrete. Cem Concr Compos 2008;30(10):898–906.
[5] Hegger J, Will N, Bruckermann O, Voss S. Load–bearing behaviour and simulation of textile reinforced concrete. Mater Struct 2006;39(8):765–76.
[6] Chudoba R, Sharei E, Scholzen A. A strain-hardening microplane damage model for thin-walled textile-reinforced concrete shells, calibration procedure, and experimental validation. Compos Struct 2016;152:913–28.
[7] Oliveira R, Ramalho M, Corrêa M. A layered finite element for reinforced concrete beams with bond–slip effects. Cem Concr Compos 2008;30(3):245–52.
[8] Lin X, Zhang Y. Novel composite beam element with bond-slip for nonlinear finite-element analyses of steel/frp-reinforced concrete beams. J Struct Eng 2013;139(12):06013003.
[9] Biscaia HC, Chastre C, Silva MA. Linear and nonlinear analysis of bond-slip models for interfaces between frp composites and concrete. Compos Part B Eng 2013;45(1):1554–68.
[10] Lin X, Zhang Y. Evaluation of bond stress-slip models for frp reinforcing bars in concrete. Compos Struct 2014;107:131–41.
[11] Monetto I. Analytical solutions of three-layer beams with interlayer slip and stepwise linear interface law. Compos Struct 2015;120:543–51.

[12] Biscaia HC, Chastre C, Silva MA. Bond-slip model for frp-to-concrete bonded joints under external compression. Compos Part B Eng 2015;80:246–59.
[13] Vilanova I, Torres L, Baena M, Llorens M. Numerical simulation of bond-slip interface and tension stiffening in gfrp rc tensile elements. Compos Struct 2016;153:504–13.
[14] Chen C, Cheng L. Theoretical solution to fatigue bond stress distribution of nsm frp reinforcement in concrete. Compos Part B Eng 2016;99:453–64.
[15] Ferreira SR, Martinelli E, Pepe M, de Andrade Silva F, Toledo Filho RD. Inverse identification of the bond behavior for jute fibers in cementitious matrix. Compos Part B Eng 2016;95:440–52.
[16] Zhou A, Qin R, Feo L, Penna R, Lau D. Investigation on interfacial defect criticality of frp-bonded concrete beams. Compos Part B Eng 2017;113:80–90.
[17] Windisch A. A modified pull-out test and new evaluation methods for a more real local bond-slip relationship. Mater Struct 1985;18(3):181–4.
[18] Naaman AE, Namur GG, Alwan JM, Najm HS. Fiber pullout and bond slip. ii: experimental validation. J Struct Eng 1991;117(9):2791–800.
[19] Banholzer B, Brameshuber W, Jung W. Analytical evaluation of pull-out tests - the inverse problem. Cem Concr Compos 2006;28(6):564–71.
[20] Murcia-Delso J, Stavridis A, Shing PB. Bond strength and cyclic bond deterioration of large-diameter bars. ACI Struct J 2013;110(4):659.
[21] Rossetti VA, Galeota D, Giammatteo M. Local bond stress-slip relationships of glass fibre reinforced plastic bars embedded in concrete. Mater Struct 1995;28(6):340–4.
[22] Pecce M, Manfredi G, Realfonzo R, Cosenza E. Experimental and analytical evaluation of bond properties of gfrp bars. J Mater Civ Eng 2001;13(4):282–90.
[23] Baena M, Torres L, Turon A, Barris C. Experimental study of bond behaviour between concrete and frp bars using a pull-out test. Compos Part B Eng 2009;40(8):784–97.
[24] Capozucca R. Analysis of bond-slip effects in rc beams strengthened with nsm cfrp rods. Compos Struct 2013;102:110–23.
[25] Vilanova I, Baena M, Torres L, Barris C. Experimental study of bond-slip of gfrp bars in concrete under sustained loads. Compos Part B Eng 2015;74:42–52.
[26] Lorenz E, Schütze E, Schladitz F, Curbach M. Textilbeton–grundlegende untersuchungen im überblick. Bet Stahlbetonbau 2013;108(10):711–22.
[27] Lorenz E, Schütze E, Weiland S. Textilbeton–eigenschaften des verbundwerkstoffs. Bet Stahlbetonbau 2015;110(S1):29–41.
[28] Dai J, Ueda T, Sato Y. Development of the nonlinear bond stress–slip model of fiber reinforced plastics sheet–concrete interfaces with a simple method. J Compos Constr 2005;9(1):52–62.
[29] DAmbrisi A, Feo L, Focacci F. Experimental and analytical investigation on bond between carbon-frcm materials and masonry. Compos Part B Eng 2013;46:15–20.
[30] Carozzi FG, Milani G, Poggi C. Mechanical properties and numerical modeling of fabric reinforced cementitious matrix (frcm) systems for strengthening of masonry structures. Compos Struct 2014;107:711–25.
[31] Carozzi FG, Poggi C. Mechanical properties and debonding strength of fabric reinforced cementitious matrix (frcm) systems for masonry strengthening. Compos Part B Eng 2015;70:215–30.
[32] Donnini J, Corinaldesi V, Nanni A. Mechanical properties of frcm using carbon fabrics with different coating treatments. Compos Part B Eng 2016;88:220–8.
[33] Barbieri G, Biolzi L, Bocciarelli M, Cattaneo S. Pull out of frp reinforcement from masonry pillars: experimental and numerical results. Compos Part B Eng 2015;69:516–25.
[34] F. G. Carozzi, A. Bellini, T. D'Antino, G. de Felice, F. Focacci, Ł. Hojdys, et al., Experimental investigation of tensile and bond properties of carbon-frcm composites for strengthening masonry elements, Compos Part B Eng.
[35] Wozniak M, Tysmans T, Verbruggen S, Vantomme J. Quality of the bond between a strain hardening cement composite stay-in-place formwork and concrete: comparison of two experimental set-ups. Constr Build Mater 2017;146:764–74.
[36] Faella C, Martinelli E, Nigro E. Direct versus indirect method for identifying frp-to-concrete interface relationships. J Compos Constr 2009;13(3):226–33.
[37] Martinelli E, Czaderski C, Motavalli M. Modeling in-plane and out-of-plane displacement fields in pull-off tests on frp strips. Eng Struct 2011;33(12):3715–25.
[38] Bilotta A, Ceroni F, Lignola G, Prota A. Use of dic technique for investigating the behaviour of frcm materials for strengthening masonry elements. Compos Part B Eng 2017;129:251–70.
[39] Lu X, Teng J, Ye L, Jiang J. Bond–slip models for frp sheets/plates bonded to concrete. Eng Struct 2005;27(6):920–37.
[40] Focacci F, Nanni A, Bakis CE. Local bond-slip relationship for frp reinforcement in concrete. J Compos Constr 2000;4(1):24–31.
[41] Saleeb A, Gendy A, Wilt T. Parameter-estimation algorithms for characterizing a class of isotropic and anisotropic viscoplastic material models. Mech Time-Dependent Mater 2002;6(4):323–61.
[42] Yun GJ, Shang S. A self-optimizing inverse analysis method for estimation of cyclic elasto-plasticity model parameters. Int J Plasticity 2011;27(4):576–95.
[43] Sinaie S, Heidarpour A, Zhao X. A multi-objective optimization approach to the parameter determination of constitutive plasticity models for the simulation of multi-phase load histories. Comput Struct 2014;138:112–32.
[44] Wozniak M, Tysmans T, Verbruggen S, Vantomme J. Nonlinear indirect identification method for cement composite-to-concrete bond. Compos Struct 2017;176:72–81.
[45] Naaman AE, Namur GG, Alwan JM, Najm HS. Fiber pullout and bond slip. i: analytical study. J Struct Eng 1991;117(9):2769–90.
[46] Liu K, Wu Y-F. Analytical identification of bond–slip relationship of eb-frp joints. Compos Part B Eng 2012;43(4):1955–63.
[47] Zastrau B, Richter M, Lepenies I. On the analytical solution of pullout phenomena in textile reinforced concrete. J Eng Mater Technol 2003;125(1):38–43.
[48] Banholzer B, Brameshuber W, Jung W. Analytical simulation of pull-out tests - the direct problem. Cem Concr Compos 2005;27(1):93–101.
[49] Yuan H, Lu X, Hui D, Feo L. Studies on frp-concrete interface with hardening and softening bond-slip law. Compos Struct 2012;94(12):3781–92.
[50] Zienkiewicz OC, Taylor RL, Zhu J. The finite element method for solid and structural mechanics. Butterworth-heinemann 2005:69–71.
[51] R. E. Goodman, R. L. Taylor, T. L. Brekke, A model for the mechanics of jointed rock, J Soil Mech Found Div.
[52] Herrmann LR. Finite element analysis of contact problems. J Eng Mech Div 1978;104(5):1043–57.
[53] Grande E, Imbimbo M. A simple 1d-finite element approach for the study of the bond behavior of masonry elements strengthened by frp. Compos Part B Eng 2016;91:548–58.
[54] Hernandez C, Ovando-Martinez R, Arjona M. Application of tensor analysis to the finite element method. Appl Math Comput 2013;219(9):4625–36.
[55] Åhlander K, Otto K. Software design for finite difference schemes based on index notation. Future Generation Computer Systems 2006;22(1):102–9.
[56] Konrad M. Effect of multifilament yarn crack bridging on uniaxial behavior of textile reinforced concrete PhD. thesis RWTH Aachen; 2008.
[57] M. Konrad, R. Chudoba, Tensile behavior of cementitious composite reinforced with epoxy impregnated multifilament yarns, Int J multiscale Comput Eng 7(2).
[58] Brent RP. Algorithms for minimization without derivatives. Cour Corp 2013.
[59] Rypl R, Chudoba R, Scholzen A, Vořechovskỳ M. Brittle matrix composites with heterogeneous reinforcement: multi-scale model of a crack bridge with rigid matrix. Compos Sci Technol 2013;89:98–109.
[60] Tanaka M, Dulikravich GS. Inverse problems in engineering mechanics. Elsevier; 1998.
[61] RILEM Technical Committee 232-TDT (Wolfgang Brameshuber). Recommendation of rilem tc 232-tdt: test methods and design of textile reinforced concrete: uniaxial tensile test: test method to determine the load bearing behavior of tensile specimens made of textile reinforced concrete. Mater Struct 2016;49:4923–7.
[62] Chudoba R, Vořechovskỳ M, Konrad M. Stochastic modeling of multi-filament yarns. i. random properties within the cross-section and size effect. Int J Solids Struct 2006;43(3):413–34.
[63] Redon C, Li VC, Wu C, Hoshiro H, Saito T, Ogawa A. Measuring and modifying interface properties of pva fibers in ecc matrix. J Mater Civ Eng 2001;13(6):399–406.
[64] Monti G, Filippou FC, Spacone E. Finite element for anchored bars under cyclic load reversals. J Struct Eng 1997;123(5):614–23.
[65] Cox JV, Herrmann LR. Validation of a plasticity bond model for steel reinforcement. Mech Cohesive-frictional Mater 1999;4(4):361–89.
[66] Lundgren K, Gylltoft K. A model for the bond between concrete and reinforcement. Mag Concr Res 2000;52(1):53–63.
[67] Lowes LN, Moehle JP, Govindjee S. Concrete-steel bond model for use in finite element modeling of reinforced concrete structures. ACI Struct J 2004;101:501–11.
[68] Delso J, Stavridis A, Shing B, Papadrakakis M, Fragiadakis M, Plevris V. Modeling the bond-slip behavior of confined large diameter reinforcing bars. III ECCOMAS thematic conf. On computational methods in structural dynamics and earthquake engineering COMPDYN. vol. 14. 2011. Corfu, Greece.
[69] Murcia-Delso J, Benson Shing P. Bond-slip model for detailed finite-element analysis of reinforced concrete structures. J Struct Eng 2014;141(4):04014125.
[70] Li Y, Chudoba R. Pyiiout - a demonstrative project of using python and index notation for efficient and consistent implementation of numerical algorithms. 2017https://github.com/simvisage/Pyiiout, Accessed date: 10 February 2017.
[71] Jirásek M, Bazant ZP. Inelastic analysis of structures. vol. 22. John Wiley & Sons; 2002. p. 399–401.